#### **BIOENGINEERING**

# Design of medical tympanostomy conduits with selective fluid transport properties

Haritosh Patel<sup>1,2†</sup>, Ida Pavlichenko<sup>1,2†</sup>, Alison Grinthal<sup>1</sup>, Cathy T. Zhang<sup>1</sup>, Jack Alvarenga<sup>1,2</sup>, Michael J. Kreder<sup>1</sup>, James C. Weaver<sup>1,2</sup>, Qin Ji<sup>2</sup>, Christopher W. F. Ling<sup>2</sup>, Joseph Choy<sup>2</sup>, Zihan Li<sup>2</sup>, Nicole L. Black<sup>1,2</sup>, Paulo J. M. Bispo<sup>3,4</sup>, Jennifer A. Lewis<sup>1,2</sup>, Elliott D. Kozin<sup>4,5</sup>, Joanna Aizenberg<sup>1,2,6\*</sup>, Aaron K. Remenschneider<sup>4,5\*</sup>

Implantable tubes, shunts, and other medical conduits are crucial for treating a wide range of conditions from ears and eyes to brain and liver but often impose serious risks of device infection, obstruction, migration, unreliable function, and tissue damage. Efforts to alleviate these complications remain at an impasse because of fundamentally conflicting design requirements: Millimeter-scale size is required to minimize invasiveness but exacerbates occlusion and malfunction. Here, we present a rational design strategy that reconciles these tradeoffs in an implantable tube that is even smaller than the current standard of care. Using tympanostomy tubes (ear tubes) as an exemplary case, we developed an iterative screening algorithm and show how unique curved lumen geometries of the liquid-infused conduit can be designed to co-optimize drug delivery, effusion drainage, water resistance, and biocontamination/ingrowth prevention in a single subcapillary-length-scale device. Through extensive in vitro studies, we demonstrate that the engineered tubes enabled selective uni- and bidirectional fluid transport; nearly eliminated adhesion and growth of common pathogenic bacteria, blood, and cells; and prevented tissue ingrowth. The engineered tubes also enabled complete eardrum healing and hearing preservation and exhibited more efficient and rapid antibiotic delivery to the middle ear in healthy chinchillas compared with current tympanostomy tubes, without resulting in ototoxicity at up to 24 weeks. The design principle and optimization algorithm presented here may enable tubes to be customized for a wide range of patient needs.



#### **INTRODUCTION**

Implanted medical tubes, shunts, catheters, stents, and other conduits have become indispensable for diverse conditions requiring controlled fluid transport, including drug delivery, fluid egress, and inter-area fluid transit for pressure normalization (1-3). Despite decades of widespread use, implantable medical conduits (IMCs) still impose serious burdens of complications on patients because of device infection, obstruction, displacement, malfunction, and frequent replacement (4-6). Various updates have attempted to mitigate such complications, but, ultimately, the problems stem from underlying and as-yet unresolved trade-offs: IMC millimeter-scale size makes it notoriously difficult to initiate and maintain steady fluid flow because of the inherent pressure barrier and frequent occlusion by adhered bacteria and cellular debris. However, minimizing IMC size is crucial, especially in highly sensitive areas such as the brain, eye, eardrum, and bile duct, where even tiny subcapillary-length-scale (namely, <2.7 mm) tubes may exacerbate tissue damage, inflammation, and incursion of fluid contaminants. Reconciling these conflicting design

requirements in a single device presents a fundamental scientific challenge, but a comprehensive solution could make a transformative difference in reducing IMC risk burden.

Tympanostomy tubes (TTs) are one of the most widely used IMCs, and complications stemming from TTs illustrate the myriad performance challenges of IMC design (Fig. 1). Implanted in the most common ambulatory pediatric surgery in the United States (with prevalence of 8.6% or 6.26 million children as of 2020) (7), TTs are used to treat otitis media (OM), or ear infections, the most frequently diagnosed childhood illness, annually accruing a cost burden of \$3 billion to \$5 billion in the United States (Fig. 1, A and B) (1, 8). The desired function of TTs is fivefold: to equalize air pressure across the tympanic membrane (TM), allow therapeutics to enter the middle ear (ME), and drain effusion out of the ME into the external auditory canal (EAC) while preventing environmental water from entering the tube and avoiding biocontamination with pathogens and cells (Fig. 1C). However, in practice, current TTs fail to consistently achieve these multipronged, largely conflicting goals (1, 9), leading to a range of complications (Fig. 1D) (10), among which the TT-induced otorrhea (ear discharge) that is often associated with a foul odor, fever, and pain is the most common complication, occurring in about 16% of children within 1 month and in 75% within 12 months (11). Other sequelae include TT occlusion (7 to 10%), myringo- and tympanosclerosis (32%), TM focal atrophy (25%), tissue granulation (5%), premature extrusion (4% with short-term TTs and 16.6% with long-term TTs), retraction pocket (3.1%), cholesteatoma (0.7%), and medial displacement (0.5%) (10).

Device miniaturization is desirable to reduce tissue damage and scarring; however, proper drainage requires widening a narrow

<sup>&</sup>lt;sup>1</sup>Harvard John A. Paulson School of Engineering and Applied Sciences, Harvard University, Boston, MA 02134, USA. <sup>2</sup>Wyss Institute for Biologically Inspired Engineering, Harvard University, Boston, MA 02115, USA. <sup>3</sup>Department of Ophthalmology, Massachusetts Eye and Ear, Boston, MA 02114, USA. <sup>4</sup>Harvard Medical School, Harvard University, Boston, MA 02115, USA. <sup>5</sup>Department of Otolaryngology–Head and Neck Surgery, Massachusetts Eye and Ear, Boston, MA 02114, USA. <sup>6</sup>Department of Chemistry and Chemical Biology, Harvard University, Cambridge, MA 02138, USA.

<sup>†</sup>These authors contributed equally to this work.

<sup>\*</sup>Corresponding author. Email: jaiz@seas.harvard.edu (J. Aizenberg); aaron\_remenschneider@meei.harvard.edu (A.K.R.)

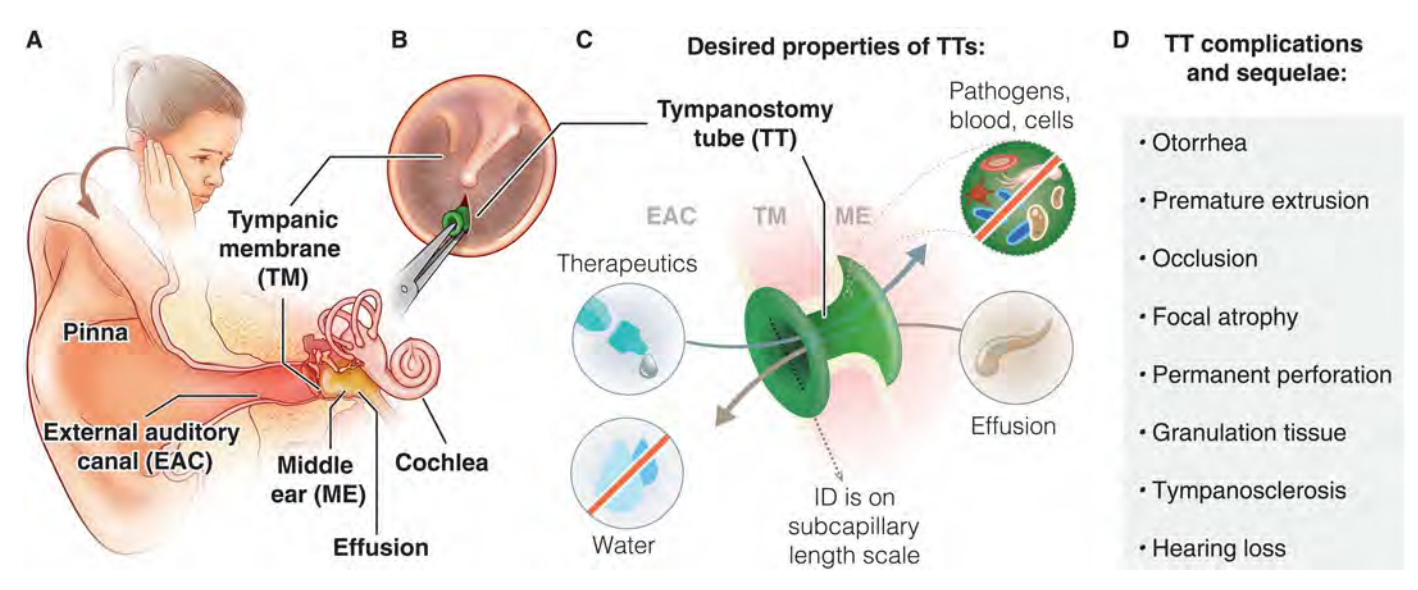


Fig. 1. Functional requirements and performance challenges in the design of tympanostomy tubes. (A) Anatomy of the ear of a patient with acute otitis media (OM). OM occurs in the middle ear (ME) space behind the tympanic membrane (TM), usually after an upper respiratory infection during which the Eustachian tubes swell, preventing air from entering the ME and resulting in fluid accumulation (or effusion) that can harbor pathogens and lead to recurrent infections and conductive hearing loss. (B) Myringotomy surgery with the insertion of a TT into the TM. (C) Schematic highlighting the desired properties of advanced TTs: small internal diameters (IDs), efficient transport of topical therapeutics from the external auditory canal (EAC) to ME, prevention of undesirable fluids from entering the ME, effective drainage of effusion from the ME, and resistance to adhesion of biocontaminants while aiming to reduce the damage to the TM tissue and ventilating the ME. (D) Complications and sequelae arising from nonideal TTs (1).

passage for efficient transport of a thick mucus or purulence without occlusion with sticky biodebris. At the same time, maintaining tube patency to the external environment for air equilibration and to maintain ME fluid drainage risks penetration of contaminant-laden water (during bathing and swimming) into the ME. To the extent that standard-of-care (SoC) TTs have been designed to resist water entry, they also make it difficult to deliver aqueous-based antibiotics, leading to inconsistent dosing that often relies on active (and at times painful) forceable manipulation of the external ear (12) or, worse, requires oral antibiotics that risk systemic side effects and promote the emergence of antimicrobial-resistant bacteria in multiple colonized body sites (1). Antimicrobial resistance and incomplete medication dosing may further exacerbate the infection, producing recurrent difficult-to-treat ME effusion (also called refractory TT otorrhea), and increasing tube occlusion, which further blocks antibiotics and incurs device-associated infection, membrane damage, and secondary hearing loss. Local tissue growth into the tube can further obstruct the tube lumen or prematurely extrude the TT, requiring repeat surgery. This vicious cycle is likely to persist without a comprehensive approach to TT design that can simultaneously optimize effusion transport, resist water and biocontamination, and facilitate aqueous drug delivery. Beyond ear infections, formulating a set of rational criteria for such multifunctional tubes is also of notable interest in the context of treating other conditions of the middle and inner ear, such as hearing loss and balance disorders (13, 14), and extending these principles to optimize IMCs for treating fluid-based conditions throughout the body.

Whereas selective fluid transport is frequently achieved by optimizing the conduit size, fluid interface chemistry, or through active gating (15-18), we hypothesized that the lumen shape can be tailored to discriminate between even chemically similar liquids. In

particular, a design featuring a curved profile would enable us to better engineer a specific capillary resistance along the tube that blocks the entry of environmental water but simultaneously allows passive delivery of ear drops while also facilitating the exit of effusion fluid (19). Here, through synergistic tailoring of materials and geometries, we demonstrated such rationally designed TTs that solve the above fluid discrimination challenges in one subcapillary-length-scale device and prevent the adhesion of pathogenic bacteria, cells, and blood yet at a smaller scale than current SoC-TT(s). The design at the material and device scales was approached as a multicriteria optimization problem inspired by the logistic regression kernel (20) that allowed for screening and selecting customized conduit geometries using the computational modeling of fluid transport through the TTs. Informed by the modeling, we fabricated TTs with selected curved lumen shapes and experimentally evaluated their performance through comprehensive characterization of materials and transport properties and extensive in vitro and in vivo studies.

#### **RESULTS**

#### Design of the tube with optimized fluid transport

Current commercially available TTs come in a variety of geometries with different internal diameters (IDs), lengths, and flange configurations (21, 22); however, they all exhibit straight-walled lumens in either cylindrical or conical form (Fig. 2A). In both cases, the conventional TT designs present a major barrier to transport, because the straight-walled lumen leads to abrupt changes in geometry at the end of the tube that, in turn, result in an abrupt change in pressure. This pressure barrier induces pinning of the transported liquid, which not only prevents therapeutic drops from eluting into the ME but often results in both therapeutic and environmental

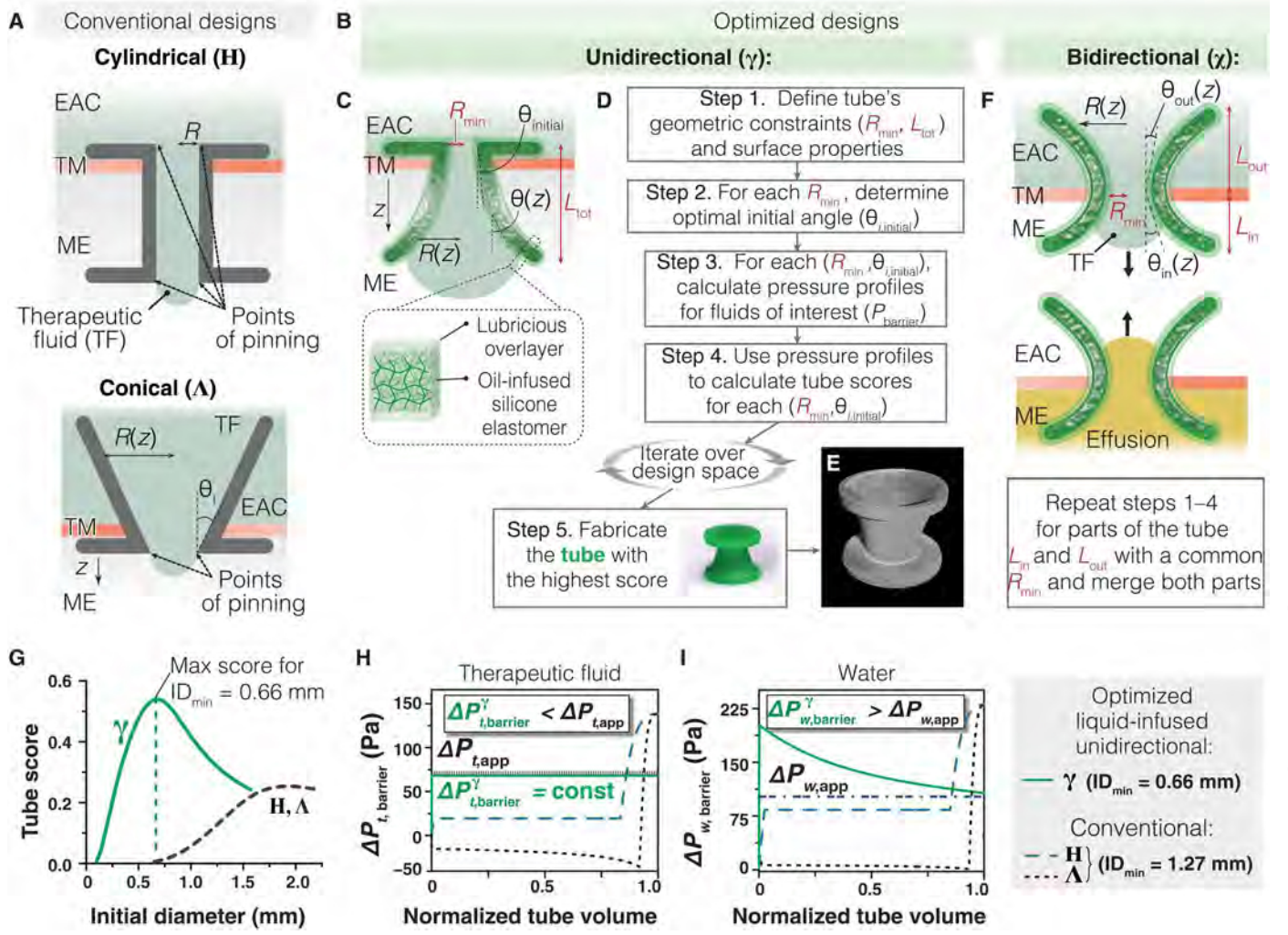


Fig. 2. Fluid transport modeling of SoC-TT and curved infused TTs. (A and B) Schematics of (A) stereotypical cross sections of lumina of conventional cylindrical (H) and conical ( $\Lambda$ ) TTs and of (B) optimized TT designs for unidirectional selective therapeutic fluid (TF) transport (denoted as  $\gamma$ ) from the EAC into the ME and for bidirectional ( $\chi$ ) transport in both (EAC $\rightarrow$ ME and ME $\rightarrow$ EAC) directions. (C) Schematic of the  $\gamma$ -TT and its critical geometric parameters; the inset shows the material of the tube: oil-infused (denoted "i") silicone elastomer with a lubricious overlayer. (D) An algorithm for constructing an optimal  $\gamma$ -TT for selective transport of therapeutics into the ME. (E) Computed tomography scan of  $\gamma$ -/TT with ID<sub>min</sub> = 0.66 mm that was optimized for transport of antibiotic/steroid combination ear drops. (F) Schematic of the  $\chi$ -TT and its critical geometric parameters for optimal transport of TF (top image) and effusion (bottom image). (G) The tube scores of  $\gamma$ -i, H-, and  $\Lambda$ -TTs with varying lumen inner diameters. (H and I) The pressure profiles of (H) TF and (I) water as they propagate through the  $\gamma$ -iTT (green solid line) and conventional TTs (blue dashed line, H-TT and black dotted line,  $\Lambda$ -TT).

fluids becoming trapped and occluding the tube (23). Moreover, molecular to microscale imperfections in the material throughout the lumen promote biological attachment and colonization on the walls (24, 25).

Here, we aimed to overcome all transport-related problems by redesigning TTs from first principles to eliminate the pressure and roughness-induced pinning of select transported liquids. The Young-Laplace (YL) equation (Eq. 1) is generally used to determine the pressure barrier faced by a fluid within a hydrophobic conduit at subcapillary length scales (26, 27)

$$\Delta p_{\text{barrier}} = \frac{2\gamma}{r} \tag{1}$$

where  $\Delta p_{\text{barrier}}$  is the pressure difference across the fluid-air

interface,  $\gamma$  is the surface tension, and r is the radius of the meniscus. However, these parameters yield little to no insight into how the conduit itself can be geometrically modified to improve transport. We thus reformulated the YL equation such that the pressure barrier is instead directly related to the material and geometry of the TT (Eq. 2, Materials and Methods S1, and fig. S1)

$$\Delta p_{\text{barrier}} = -\frac{2\gamma_{\text{eff}}}{R(z)}\cos(\theta_{\text{adv}} + \theta_{\text{l}}(z)) \tag{2}$$

where  $\gamma_{\rm eff}$  is the effective surface tension determined by spreading coefficient behavior (28),  $\theta_{\rm adv}$  is the advancing angle of the three-phase front, R is the radius of the tube, and  $\theta_{\rm l}$  is the lumen flare angle. By explicitly relating the pressure to two complementary geometric parameters, Eq. 2 suggests that geometric pressure barriers

can be avoided by continuously covarying the radius and lumen angle (which specify the local curvature) from entrance to exit to keep the pressure constant—and thus avoid pinning—as a fluid travels through and exits the tube. At the same time, the reformulation highlights that the overall pressure barrier can be further reduced with a material that minimizes the effective surface tension,  $\gamma_{\rm eff}$ . This second point can be optimally met with liquidinfused materials—a bioinspired strategy in which a porous solid is infused with an omniphobic oil to create a molecularly smooth, nonsticky liquid interface (29–31)—that exhibit minimal contact angle hysteresis and eliminate roughness-induced pinning (32–34) while, at the same time, preventing biological attachment (35–38), which leads to occlusion, pathogenicity, and device extrusion.

To comprehensively optimize the lumen geometry, we developed an iterative screening algorithm that numerically solves Eq. 2 at each point to define parameters that maintain constant pressure all along the path for tubes designed for selective uni- and bidirectional flow (Fig. 2B). Figure 2C presents a schematic of an exemplary tube (with the parameters indicated), denoted as γ-TT, designed for unidirectional transport, for example, for antibiotic delivery into the ME. The sequence of steps that the algorithm uses to arrive at an optimized geometry is outlined in Fig. 2D (Materials and Methods S2), and the tube with the highest score is selected for fabrication (Fig. 2E). Although specifying a transport liquid (for example, therapeutic) determines the specific curvature of the lumen (fig. S2), the overall form factors of the tube such as length  $(L_{tot})$  and entrance radius  $(R_{\min})$  are still free to be optimized for other requirements of the TT such as selectivity (fig. S3), hence allowing antibiotics transport but preventing water entry.

To create a unique two-way tube that enables explicit tailoring of both effusion drainage and therapeutic delivery, the unidirectional algorithm can be extended to satisfy the conditions for bidirectional transport simply by independently optimizing two  $\gamma$ -tubes—one for inward and one for outward transport—and connecting them with a common inner radius to form an hourglass shape, denoted as  $\chi$ -TT (Fig. 2F). The fraction of the tube length tailored for inward ( $L_{\rm in}$ ) and outward ( $L_{\rm out}$ ) transport must still sum to the same  $L_{\rm tot}$ . The ability to vary the portion of the tube devoted to inward or outward optimization introduces a new partition parameter, defined as  $L_{\rm in}/L_{\rm tot}$ , that can be adapted for specific patient conditions. The TTs are now screened for various radii and partitions to determine an ideal tube using the same scoring formulation as before.

For this study, the following parameters were used (tables S1 and S2).  $L_{\text{tot}}$  was set to 2.3 mm to stay comparable to the conventional designs, specifically to the chosen silicone SoC-TTs used as controls (Sheehy Collar Button from Summit Medical, model no. VT1002), and to remain within anatomical constraints. For the tube material, we chose silicone, the same material used in SoC-TTs, but infused with a medical-grade silicone oil (to differentiate from the "noninfused" tubes, the oil-infused tubes are denoted *i*TTs hereafter). The liquids studied were the combination antibiotic/steroid ear drops (0.3% ciprofloxacin and 0.1% dexamethasone suspension)  $(\gamma = 44 \text{ mN m}^{-1})$ , exogenous water  $(\gamma = 72 \text{ mN m}^{-1})$ , and synthetic mucin to represent effusion solution. The applied transport pressure was defined as the pressure exerted by a millimeter-sized droplet of either therapeutic,  $\Delta p_{t,app} = 70$  Pa (fig. S4), or water,  $\Delta p_{w,\text{app}} = 100 \text{ Pa}$  (fig. S5). The radius was swept between 50 and 750 µm. The unidirectional algorithm was used to screen for the

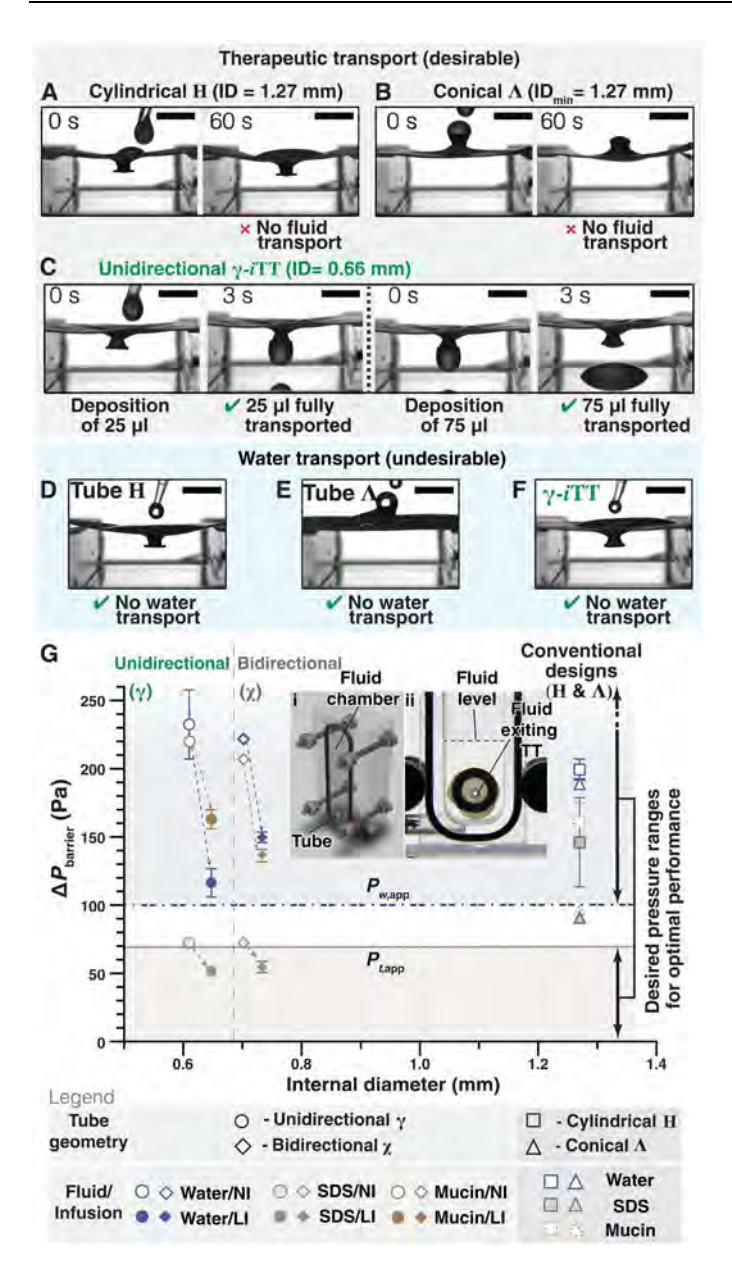
optimal  $\gamma$ -iTT for inward transport without pinning (Materials and Methods S3 for discussion), with equal objective weight given to transporting therapeutics, resisting water, and maximizing water/antibiotic discrimination. Figure 2G displays the tube score results: The optimal  $\gamma$ -iTT has an ID of 0.66 mm, about half that of the SoC-TT (1.27 mm). For bidirectional transport, the optimal  $\chi$ -iTT design has an inner proximal diameter of 0.69 mm and a partition of 0.29 (Materials and Methods S4 and figs. S6 and S7).

Figure 2 (H and I) shows the simulated pressure profiles of therapeutics and water, respectively, from entrance to exit within the conventional cylindrical (H) and conical ( $\Lambda$ ) tubes and optimized curved  $\gamma$ -iTT designs. Simulated results show that the  $\gamma$ -iTT satisfies the criteria for selective, passive drug transport; namely,  $\Delta p_{t,app}$ can overcome the pressure barrier,  $\Delta p_{t,\text{barrier}}$ , resisting its transport  $(\Delta p_{t,\text{barrier}} \leq \Delta p_{t,\text{app}} = 70 \text{ Pa})$ , whereas  $\Delta p_{w,\text{app}}$  is below the pressure barrier, resisting water entry into the tube,  $\Delta p_{w,\text{barrier}}$  ( $\Delta p_{w,\text{barrier}}$  $\geq \Delta p_{w,app} = 100 \text{ Pa}$ ). In contrast, the conventional tubes show good resistance to water transport but have pressure barriers well beyond the desired range for therapeutic transport and thus are not expected to passively transport drugs. The optimized γ-iTT is then manufactured using custom three-dimensional (3D)-printed molds and subsequent infusion with a medical-grade silicone oil, resulting in an isotropic 10% swelling of the TT's dimensions (Materials and Methods S5 and fig. S8).

#### Fluid transport experiments

The simulations shown in Fig. 2 (H and I) accurately predict the experimentally observed transport behavior of the conventional (H-TT and  $\Lambda$ -TT) and curved ( $\gamma$ -iTT) designs. Otic drops were unable to transport through the conventional designs (Fig. 3, A and B), indicating that  $\Delta p_{t,\mathrm{app}} < \Delta p_{t,\mathrm{barrier}}$ . In contrast, the  $\gamma$ -iTT passively transported each droplet completely in 3 to 5 s (Fig. 3C), demonstrating that the design satisfies  $\Delta p_{t,\mathrm{app}} > \Delta p_{t,\mathrm{barrier}}$ . The conventional and curved TTs were all effective in resisting the transport of water (Fig. 3, D to F), satisfying  $\Delta p_{w,\mathrm{app}} < \Delta p_{w,\mathrm{barrier}}$ . Note that the noninfused  $\gamma$ -TT did not transport either water or otic drops.

The pressure barriers for antibiotics, water, and effusion measured using a hydrostatic pressure chamber (Fig. 3G, Materials and Methods S6, and fig. S9)—here defined as the breakthrough pressures—are likewise consistent with the simulations. For the designs of  $\gamma$ - and  $\chi$ -*i*TTs, the breakthrough pressure for aqueous SDS solution (7.91 mM), which has identical relevant physical properties to ciprofloxacin/dexamethasone drops (Materials and Methods S7 and fig. S10), is lower than the typical applied pressures of the rapeutic droplets (<70 Pa), whereas, for H-TT and  $\Lambda$ -TT, the breakthrough pressures are 140 and 90 Pa, respectively, well above the desirable range. This demonstrates that therapeutics will transport without external forces such as tragal pumping through γ-iTT but will not flow passively through SoC-TTs (movie S1). Hydrostatic pressure measurements reveal a number of transport properties of note: The low  $\Delta p_{t,\text{barrier}} < 70$  Pa for *i*TTs was observed despite the fact that the minimum diameters of the curved *i*TTs are almost two times smaller than the ID of the straight-walled SoC-TTs; the curved-wall geometry of the noninfused γ- and χ-TTs alone leads to a ~50% decrease in  $\Delta p_{t,\text{barrier}}$  relative to the SoC-TT, whereas the liquid overlayer in iTTs synergizes with the geometry to bring  $\Delta p_{t,\text{barrier}}$  below  $\Delta p_{t,\text{app}}$ . In addition, without explicit optimization for outward transport, the unidirectional γ-iTT transports a 5%



**Fig. 3. Experimental in vitro evaluation of SoC-TT and curved designs.** (**A** to **C**) Optical images of 25 μl of otic droplets added onto (A) Collar Button (H-TT, ID = 1.27 mm), (B) Baxter Beveled ( $\Lambda$ -TT, ID<sub>min</sub> = 1.27 mm), and (C) optimized γ-*i*TT (ID<sub>min</sub> = 0.66 mm). Conventional tubes revealed no transport of the therapeutic within 60 s, whereas γ-*i*TT transports droplets within 3 to 5 s. (**D** to **F**) Optical images of 25 μl of water droplets added onto (D) H-TT, (E)  $\Lambda$ -TT, and (F) γ-*i*TT, confirming resistance to water permeation. Scale bars, (A to F) 5 mm. (**G**) Hydrostatic breakthrough pressure measurements of optimized not-infused (NI) and liquid-infused (LI) γ- and χ-TTs and conventional H- and  $\Lambda$ -TTs. The inset shows the schematic of the fluid chamber used for the experiments (i; movie S1) and photo of the chamber filled with a fluid exiting through the TT (ii).

mucin suspension, used as an analog for effusion fluid (fig. S11), as effectively as the SoC-TT (pressure barrier of ~160 Pa in both cases), and the bidirectionally optimized  $\chi$ -iTT demonstrated an even lower pressure barrier (~135 Pa) for mucin yet maintained a ~60% reduction in  $\Delta p_{t,\text{barrier}}$  compared with the SoC-TT. We note that the latter would translate to improved effusion drainage and lower pressure buildup in the inflamed ME. Overall, we identified that the presence of the lubricious overlayer alone leads to a ~15% reduction in  $\Delta p_{t,\text{barrier}}$  as compared with a more prominent drop in  $\Delta p_{t,\text{barrier}}$  of ~70% due to change in geometry for TTs of the same ID<sub>min</sub> (fig. S12). Note that in the context of the ear, the TTs were exposed only to small-volume intermittent fluid flow; however, the optimized iTTs maintained high performance and longevity of their fluid transport capabilities in the artificial accelerated lubricant-depletion regime (Materials and Methods S8) and were able to recover any slight loss of performance via a simple single-oil-drop replenishment step (fig. S13).

#### Biological adhesion and growth

It has been shown that the dynamic liquid interface present on the liquid-infused materials not only improves transport properties but also resists nearly all biological attachment and colonization mechanisms (37–41). Here, we tested the ability of the medical-grade silicone oil-infused silicone elastomer to repel bacteria and blood, particularly the pathogenic biofilms that underlie the widespread problem of device-associated infections (42), and to prevent attachment and ingrowth of human tissue on or in the tube, potentially avoiding the device rejection that now leads to repeated surgeries.

We studied the in vitro adhesion of the five most common pathogens isolated from patients with acute OM: methicillin-resistant Staphylococcus aureus (MRSA), Pseudomonas aeruginosa (PA), Streptococcus pneumoniae (SP), Moraxella catarrhalis (MC), and nontypeable Haemophilus influenzae (NTHI) (43–45). The optical density (OD;  $\lambda = 570$  nm) of crystal violet (CV) solubilized from stained biofilms grown in medical-grade silicone discs demonstrated a significant ~10-fold reduction in biofilm formation on the oilinfused material (Fig. 4, A to E; see P values in table S3). These results were corroborated by confocal microscopy imaging of bacteria adhered to noninfused and oil-infused (350 cP) sheets (Fig. 4F). The oil-infused sheets showed a significant ~25-fold reduction in adhered biofilm compared with noninfused sheets: The average optically observed biofilm coverage on noninfused silicone sheets was  $9.5 \pm 4.73\%$ , whereas the oil-infused samples had only 0.38  $\pm$  0.47% (P < 0.01, table S4). Furthermore, biofilms of MRSA and PA-the strains that cause difficult-to-treat recurrent OM and TT otorrhea—were incubated directly on SoC-TT, γ-TT, and γ-iTT (Fig. 4, G and H). γ-iTTs demonstrated ~2-log and ~1.5log reduction of colony-forming units (CFUs) per milliliter of MRSA and PA, respectively, as compared with SoC-TTs (CFU counts reported in table S5). Oil-infused TTs still remained highly efficacious at resisting bacterial adhesion and biofilm formation even with slightly deteriorated lubriciousness over time (Materials and Methods S9). Infused TTs also showed minimal biofouling by blood (Materials and Methods S10 and fig. S14).

We characterized the ability of the same oil-infused materials to resist the in vitro adhesion and ingrowth of epithelial tissue by incubating them for 48 hours in a culture of human epidermal keratinocytes (HEKs) and human neonatal dermal fibroblasts (HNDFs), which correspond to the outer and middle layers of the TM. The oil-

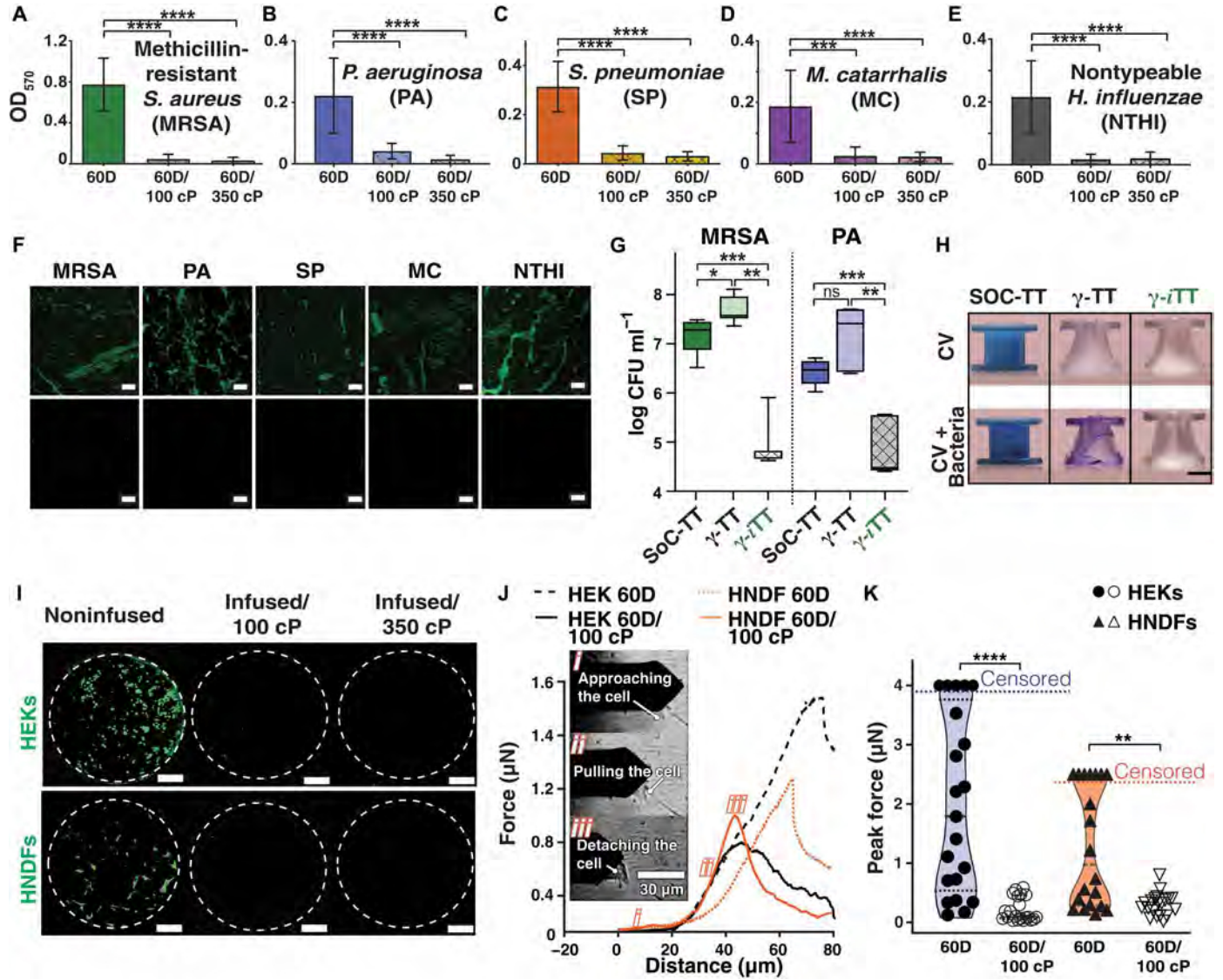


**Fig. 4. Assessment of liquid-infused material to reduce biological attachment.** (**A** to **E**) ODs of biofilms removed from the noninfused silicone sheets (60D durometer) and infused with 100 cP (60D/100 cP) and 350 cP (60D/350 cP) silicone oils (n = 9). (**F**) Syto-9 staining of biofilms confirms attachment of bacteria to the noninfused silicone (top row, green live channel) compared with the minimal adhesion to infused silicone (60D/350 cP) (bottom row). Scale bars, 20 μm. (**G**) A box-and-whisker plot of log reduction of MRSA and PA on the SoC-TT, γ-TT, and γ-iTT. (**H**) Photographs of CV-stained biofilms on the SoC-TT, γ-TT, and γ-iTT incubated for 24 hours without (top row) and with MRSA (bottom row). Scale bar, 1 cm. (**I**) Representative fluorescent images of HEKs (top row) and HNDFs (bottom row) confirming minimal adhesion to infused/100 cP and infused/350 cP flat sheets as opposed to noninfused ones after 48 hours. Scale bars, 500 μm. (**J**) Peak forces required to detach HEK and HNDF cells from the surface with an AFM cantilever. The inset shows three stages of the cell detachment, namely, (i) the cantilever first approaches the cell, then (ii) pulls the cell from the surface, resulting in an increase of force, and (iii) detaches the cell. (**K**) Peak forces required to remove HEKs and HNDFs from noninfused (60D) and oil-infused (60D/ 100 cP) silicone sheets (n = 9). Significance set at \*P < 0.05, \*\*P < 0.01, \*\*\*P < 0.001, and \*\*\*\*P < 0.0001.

infused flat silicone sheets exhibit substantially reduced adhesion of HEKs and HNDFs compared with noninfused silicone sheets (P < 0.0001 for HEKs and P = 0.002 for HNDFs; Fig. 4I). The noninfused sheets had nearly 50% cell coverage, whereas samples infused with the 100 and 350 cP oil showed attached cells at only a few locations. Moreover, the oil-infused samples showed a ~90% reduction in the force required to detach both HEKs and HNDFs adhered to the surface, as measured by the atomic force microscopy (AFM) cantilever pull-off method (Fig. 4, J and K). Oil-infused silicone also greatly limited the deposition of fibronectin (fig. S15),

which is associated with the TM inflammatory response that can lead to biofilm formation, myringitis, and rejection of the device (46, 47).

#### **Preclinical studies**

Because the innate immune response and the complex interplay between myringotomy and tube implantation cannot be captured by in vitro or computational models, we conducted preclinical in vivo studies in long-tailed chinchillas (*Chinchilla lanigera*), the gold standard model for ME and OM research. In our multipurpose

study, we assessed the safety and efficacy of the iTTs by confirming the surgical handleability, biocompatibility, absence of ototoxicity, and short-term risk of spontaneous extrusion of H-iTT and  $\gamma$ -iTTs, as well as by comparing the efficacy of drug transport through  $\gamma$ -iTTs with that of SoC-TTs in a healthy chinchilla model.

To establish the biocompatibility and otic safety profile, we implanted the control SoC-TTs ( $n_{\text{tubes}} = 16$ , where  $n_{\text{tubes}}$  is the number of tubes) and the test *i*TTs—either the  $\gamma$ -*i*TTs ( $n_{\text{tubes}} = 6$ ), with the dimensions similar to SoC-TT, or optimized  $\gamma$ -iTTs ( $n_{\text{tubes}} = 10$ ) in contralateral ears of the same chinchilla (total n = 16, where n is the number of animals; see Materials and Methods S11 and fig. S16). First, we monitored whether surgically placed iTTs caused local or regional tissue damage, including focal atrophy resulting in nonhealing of implanted TMs, tissue granulation, infection, and local scarring such as myringosclerosis in all animals. After placement of TTs via transcanal endoscopic myringotomy and tube insertion, we observed that both TMs sealed around the TTs within 2 weeks. Serial otoscopic imaging confirmed the absence of erythema, TM inflammation, and fluid accumulation in all ears after TT insertion. No tubes spontaneously extruded or became displaced over this period. TTs were endoscopically removed from the TM via the ear canal at 2 weeks after implantation. We also examined the

intrinsic regenerative capacity of the TM for 12 (for n = 6, with SoC-TTs and H-iTTs) or 24 (for n = 2, with SoC-TTs and yiTTs) weeks after tube removal; we found no difference in the rates of TM healing by tube type. Representative hematoxylin and eosin (H&E)-stained sections of healed TMs of a chinchilla obtained 12 weeks after the removal of previously implanted TMs, with the SoC-TT in the left TM and the H-iTT in the right TM are shown in Fig. 5 (A and B), respectively. TM thickening (myringosclerosis) was observed in the left TM 12 weeks after explantation of the SoC-TT (Fig. 5A) but not in the H-iTT-implanted TM (Fig. 5B). Quantitative comparison revealed that in five of the five animals, the TM that had the SoC-TT was significantly (38 to 300%) thicker as compared with the H-iTT, which exhibited fibrosis-free healing (P values reported in table S6). Second, we confirmed the lack of ototoxicity of iTTs for the inner ear by qualitative analysis of cochlear histology (fig. S17) in 12 animals euthanized at 12 or 24 weeks, previously implanted with SoC-TTs ( $n_{\text{tubes}} = 12$ ), H-iTTs  $(n_{\text{tubes}} = 5)$ , and  $\gamma$ -*i*TTs  $(n_{\text{tubes}} = 7)$  for 2 weeks. In both SoC-TTs and iTTs, implanted ears were healthy without notable losses.

Last, the otic safety of the TTs for the middle and inner ear was also confirmed by tracking hearing thresholds in implanted animals via auditory brainstem response (ABR) measured in healthy

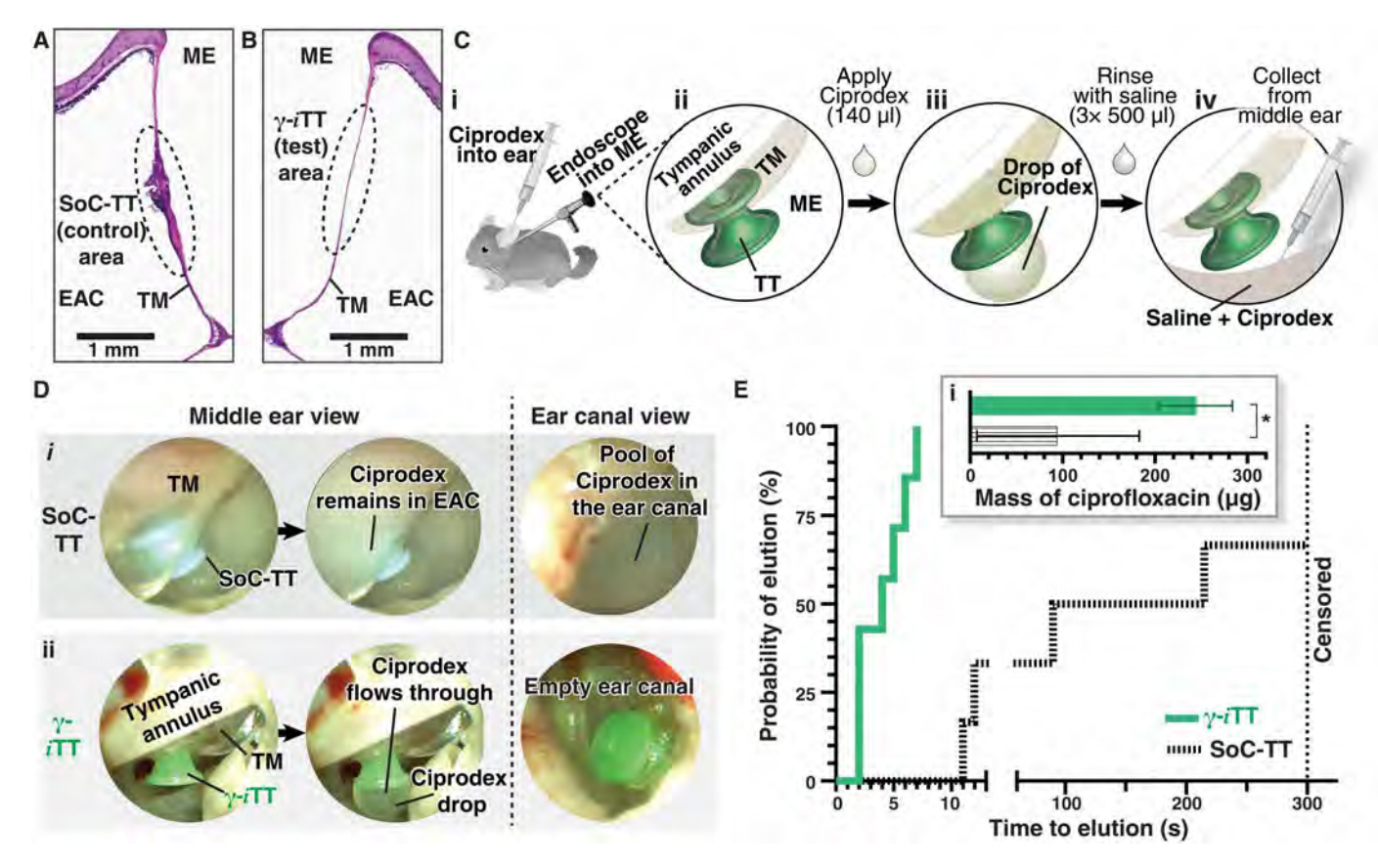


Fig. 5. Chinchilla preclinical safety and efficacy trials. (A and B) Representative H&E-stained sections of healed TMs of a chinchilla, processed ~12 weeks after the explantation of TTs, demonstrate complete healing of the TM for both (A) SoC-TT and (B) H-/TT. (C) A schematic of a study to assess the drug transport efficacy in chinchillas. Through an opening in the posterior bulla of an anesthetized animal, an endoscope was inserted into the ME space (i) to permit direct visualization of otic drops introduced with a syringe into the EAC and flowing through the TT into the ME from the EAC (ii and iii). After 5 min, the ME fluid was aspirated for HPLC characterization (iv). (D) Ciprofloxacin/dexamethasone elution through (i) SoC and (ii)  $\gamma$ -/TTs, as seen from within the ME (left box) and EAC (right box). (E) Kaplan-Meier survival estimates of probability of elution of a droplet through the TTs at various times within observation time cutoff of 5 min. The inset (i) shows the mass of ciprofloxacin extracted from the chinchilla's ME bulla as a result of drug transport through TTs ( $\gamma$ -/TT is shown in green, and the SoC-TT is shown in gray).

normal-hearing chinchillas (n=8 in arm 1 and n=5 in arm 2; Materials and Methods S11) with contralaterally inserted SoC-TTs ( $n_{\rm tubes}=8$ ) and either H-iTTs ( $n_{\rm tubes}=6$ ) or  $\gamma$ -iTTs ( $n_{\rm tubes}=2$ ) at various points: preimplantation, 2 weeks after implantation (before TT removal), and around 12 (for all TTs) or 24 (for the group with SoC-TTs and  $\gamma$ -iTTs) weeks after explantation. ABR thresholds in SoC-TT and curved iTTs ears did not demonstrate changes from before to after implantation, nor were there differences in chinchillas' hearing thresholds at 12 or 24 weeks after explantation (fig. S18).

The drug transport efficacy of the  $\gamma$ -iTTs was assessed and compared with SoC-TTs within the physiological environment of the chinchilla ear in the absence of pathogenic bacteria or infection. As shown in previous clinical trials (12), antibiotic drops do not spontaneously enter SoC-TTs; hence, patients are recommended to serially compress the cartilaginous ear canal (termed tragal pumping) and lie with their ears upright for at least 1 min after drug administration to coerce some portion of therapeutics to enter the ME. Therefore, the goal of this study was to test the superiority of the γ-iTT for improving drug transport reliability and efficacy, specifically by increasing the amount of the active drug component, ciprofloxacin, transported to the ME without tragal pumping, and within less than 1 min. As schematically shown and described in Fig. 5C, we developed a method for directly visualizing the drug transport process within the ME using an endoscope, allowing temporal resolution of fluid transport and quantification of the drug concentration in the ME fluid. The yiTT and SoC-TT were each implanted into the TMs of eight healthy chinchillas. After the TM was healed (2 weeks), we first confirmed that normal saline did not transport through either TT within 5 min of observation, and then 140 µl of drug (Ciprodex, 0.3% ciprofloxacin, and 0.1% dexamethasone otic suspension) were introduced into the EAC and allowed to drain through the TT into the ME (Materials and Methods S12 and fig. S19). The dosing of 140 µl is consistent with Food and Drug Administration-approved guidelines for ciprofloxacin/dexamethasone otic suspensions. The transport process was recorded for 5 min using a 30°-angled endoscope positioned through the animal's bulla to view the ME. After 5 min, drug delivered to the ME was extracted and analyzed by high-performance liquid chromatography (HPLC) and mass spectroscopy (MS) to determine the final ciprofloxacin content in the ME after observation (Materials and Methods S13). Figure 5D shows snapshots of the drug-transport process in SoC-TTs and  $\gamma$ -iTTs. As seen in the two representative images in the left box (from within the ME), the ciprofloxacin/dexamethasone suspension did not flow through the SoC-TT within 5 min of observation, whereas it readily flowed through the  $\gamma$ -iTT within the first 5 s in the same animal. Simultaneous endoscopic visualization of the EAC (Fig. 5D, right box) confirmed these findings, showing a pool of therapeutic drops remaining in the ear canal above the SoC-TT, in contrast to an empty ear canal above the γ-iTT. On the basis of the recorded elution times of the first drop, we estimated the probabilities of droplet elution using Kaplan-Meier survival curves (Fig. 5E). The experimental observation time cutoff was 5 min, after which the data were censored (movie S2). The first droplet exiting the y-iTT without tragal pumping was 4 s, which is 38 times faster than 152 s for the SoC-TT on the basis of median survival statistics (hazard ratio, 5.272; 95% confidence ratio, 1.345 to 20.67; P = 0.0003 was calculated using the log-rank test). On the basis of HPLC and MS analysis (fig. S20), the mass of ciprofloxacin

transported into the ME was ~95  $\pm$  90  $\mu$ g for the SoC-TT and ~240  $\pm$  45  $\mu$ g for the  $\gamma$ -iTT (Fig. 5E, inset i). Hence, nearly 60% of the full dose of ciprofloxacin, corresponding to 140  $\mu$ l of ciprofloxacin/dexamethasone suspension, was transported effectively through the  $\gamma$ -iTT in under 10 s, as opposed to only 22% delivered over 5 min for the SoC-TT. This quantitative method of assessing the efficacy of passive drug transport provides evidence of the superior drug transport capabilities of the  $\gamma$ -iTT (P < 0.05).

#### **DISCUSSION**

We have developed a comprehensive strategy that makes it possible to transport therapeutics, drain effusion, block water, prevent biocontamination and tissue ingrowth, and minimize size—long seen as competing criteria—in a single subcapillary-length-scale device. This integrated approach avoids the complications of current IMCs a priori through rational design that synergizes tailored curved lumen geometries with advantages presented by liquid-infused materials and an iterative screening algorithm. The tube is kept clear of occlusion, and, because of the curvature-specified pressure profile, both effusion and therapeutics transit through and exit the tube completely while water is stopped at the entrance, preventing any fluids from becoming trapped inside as in traditional designs. The liquid-infused material not only enhances these transport effects but also provides a unique liquid interface that is nearly impossible for bacteria and native tissue to adhere to or grow on. In particular, compared with silicone materials now used in conventional TTs, the oil-infused silicone sheets demonstrate a ~10-fold reduction in biofilm biomass assessed by OD measurements, a ~25-fold reduction in adhered biofilm assessed by confocal microscopy imaging for the five most common pathogens found in patients with acute OM and OM with effusion (PA, MRSA, SP, MC, and NTHI), and ~1.5-log and ~2-log reductions for PA and MRSA biofilm formation, respectively, on oil-infused TTs compared with SoC-TT based on CFU plating, an improvement even against the newer TiO<sub>2</sub> coating approaches on TiNi TT stents (48). These results suggest that such iTTs should not experience bacterial adhesion that underlies widespread secondary, recurrent, or biofilm-associated infections across a range of implantable devices. In addition, it is not uncommon to expose the TT to blood at the time of placement, which may result in obstruction or a higher risk of biofilm formation of PA (49). Thus, the qualitatively reported blood repellency is a tangential benefit of our material system, yet a future evaluation of antithrombogenic properties would be necessary for other IMCs with prolonged and substantial blood contact. Furthermore, the in vitro study of the adhesion and ingrowth of human epidermal keratinocytes (HEKs) and human neonatal dermal fibroblasts (HNDFs) showed nearly no attachment of cells to infused samples and a ~90% reduction in the force required to detach the adhered cells. These results support that the oil-infused iTTs mitigate cell-mediated ingrowth by preventing the initial stages of cell adhesion and extracellular matrix deposition (37). We anticipate that the reduced force necessary to detach the few cells that do adhere will enable the clearance of the iTT lumen with relative ease, for example, along with the administration of ear drops. Furthermore, our immunocytochemistry assessment of fibronectin expression in fibroblasts—and its correlation to in vivo investigation of potential postimplant scarification—shows reduced fibronectin attachment to oil-infused silicone compared

with silicone material now used in conventional TTs. We note that fibronectin, a key extracellular matrix protein, serves as an important protein implicated in cell adhesion and fibroblast differentiation, proliferation, and migration (50, 51). In particular, reduction of endogenous fibronectin has previously been shown in mouse embryonic stem cells to decrease cell adhesion, integrin signaling, and expression of self-renewal markers (52). Furthermore, tympanosclerosis and cholesteatoma formation may develop secondary to recurrent OM and, in instances, as pathological sequelae of TT implantation. Multiple lines of evidence have demonstrated that the reduction of fibroblast recruitment and adhesion can reduce pathological remodeling and the formation of tympanosclerotic plaques (53, 54). These high-performing features considerably surpass SoC-TTs, exhibiting maximal transport selectivity while avoiding pathogenic biofilms, blood, and cell growth in vitro and enabling complete rapid healing and highly efficient drug delivery (nearly the entire dose within a few seconds) in the preclinical animal studies.

Described advances from the present study come from our approach to conduit design. Whereas previous tube improvements modified traditional straight-walled tubes by introducing a small curved flare at the end, this strategy does not solve the basic problem of an abrupt pressure increase at or near the exit, which effectively maximizes the elution barrier and promotes pinning. We instead used a computational algorithm designed to generate a constant pressure throughout the entire tube by iteratively engineering the local curvature and eliminating the elution barrier while simultaneously varying the geometric parameters to maximize the discrimination between two given fluids without compromising transport efficiency for even smaller tube diameters. The use of a liquid-infused material directly unites these geometry-defined transport criteria with prevention of device contamination, colonization, in-growth, extrusion, and scarring. Our holistic design algorithm may potentially enable TTs to be customized for an individual patient's current conditions, treatment needs, prior ear history, ear anatomy, and for either inward or outward transport. At one extreme, if, for example, the tube is primarily needed for therapeutic delivery, then a y-shaped conduit could allow the fine-tuning of the selectivity profile, potentially defining a spectrum of drugs for treatment to be adapted over time. Even without further optimization, such a tube already outperforms traditional TTs for effusion drainage as well, should effusion develop after the initial assessment. In cases where drainage is the primary need, moving the minimum radius inward could allow increasing priority to be given to tailoring for a patient's specific range of effusion characteristics.

Ultimately, this complete design overhaul enables TTs to be reconceived as personalized, multifunctional devices that can potentially transform the treatment of ear disorders. In preclinical studies reported here, the γ-*i*TTs showed at least two to three times dosing increase in passive drug transport efficacy. In real terms, this results in a more efficient and rapid delivery of a prescribed dose of therapeutic drops that reach the ME within seconds as opposed to SoCTTs, which offer no passive transport in most cases, or transport on a medically impractical time scale of minutes. Furthermore, our animal studies demonstrate the absence of TM inflammation, infection, and fluid accumulation after TT insertion and excellent regenerative capacity of the TM with no regional tissue damage, granulation, or erythema at the tympanostomy site after complete healing of the TM in all animals. Note that our histology results

showed no signs of myringosclerosis in iTT-implanted TMs after healing but did show thickening of the TMs for the SoC-TT, likely attributable to the ability of liquid-infused materials to reduce fibronectin accumulation, facilitate its detachment from surfaces (38), and ameliorate fibrosis (55). Potentially, combined with curved smooth-walled geometry, liquid-infused materials may be able to further reduce foreign body response (56). Other contributing factors to minimal damage to the TM that are yet to be studied include the smaller minimal outer diameter of the γ-iTT (0.66 mm versus 1.27 mm for the SoC-TT) and its softer flanges that lead to a smaller TM orifice after explantation. Our animal studies also show stable hearing thresholds at 3 and 6 months after implantation, with preserved cochlear cellular integrity and spiral ganglion neuron populations. Together, these results demonstrate the unique ability of these tubes to easily and reliably dose antibiotics into the ME, keep out environmental water, prevent clogging and infectious buildup, avoid scarring, and keep the tube clear for aeration and pressure stabilization, all in the context of miniaturization of tube dimensions. Such evidence provides a multipronged approach for circumventing the frustrating cycle of complications that often plagues TT use.

More broadly, the design strategy presented in this work serves as a foundation that can be adapted for rationally designing other IMCs such as catheters, shunts, and tubes that also often suffer from unsteady flow and biodebris accumulation. In particular, the fundamental principles for using tailored curvature to optimize flow efficiency and selectivity can be translated to the many IMCs where flow is driven by pressure differences, with particular promise for the smallest IMCs, such as brain, eye, and biliary tubes, where the threshold pressure to initiate transport and clearance could be substantially reduced even at subcapillary length scales. Using liquidinfused materials for these applications can also minimize pinning and bioadhesion throughout even the longest conduits, where liquid trapping and pathogenic biofilm growth are extremely difficult to prevent or remedy. The approach presented here can be applied to reverse-engineer drug properties for optimal transport, uniting device design with drug discovery and formulation. Manufacturing such miniature IMCs can be addressed via careful optimization of the conventional micromold designs (for example, with ultrafast laser micromanufacturing, microprecision 3D printing, or microstereolithography) and liquid silicone rubber injection parameters (57). In summary, the multiscale geometry-material synergy and physics-based optimization algorithm offer promise for rethinking IMC design to ease much of the burden of complications that have previously been considered inevitable while envisioning multifunctional approaches to treating fluid-based conditions throughout the body.

#### **MATERIALS AND METHODS**

#### Study design Ex vivo studies

Our experiments compared the biofilm and human cell adhesion with noninfused and infused silicone discs as well as to control SoC-TTs and test  $\gamma$ -iTTs. The bacterial study was approved by the Massachusetts General Brigham Institutional Review Board. Clinical isolates of MRSA, PA, SP, MC, and NTHI were recovered from patients with chronic OM seen at the Massachusetts Eye and Ear (Boston, MA). For the bacterial study, a sample size of n = 9 discs

for each cell type was chosen, which would provide 95% power to detect 90% relative differences in the mean OD measurements for the noninfused and infused silicone discs, and n=3 would provide 80% power to detect 90% relative differences in the mean CFU counts for SoC-TTs and  $\gamma$ -iTTs at a 0.05 significance level based on power analysis using the two-sample t test, which was supported by our published experience (37, 39). For the AFM experiments with cells, a sample size n=3 sheets per cell type (with six or seven cells measured per sheet) was chosen to provide 95% power to detect a 90% relative difference in cellular adhesion to noninfused and infused silicone discs using a two-tailed Wilcoxon-Mann-Whitney test (population medians) with a 95% confidence interval, which was supported by our published experience (41).

#### In vivo studies

Our primary objective was to compare the efficacy of drug transport through γ-*i*TTs and SoC-TTs within the physiological environment of a healthy chinchilla ear. Our secondary objective was to assess biocompatibility and absence of ototoxicity of iTTs by monitoring the TM healing process and measuring the ABR responses (see Materials and Methods S11 for more details). The animal efficacy study performed at CBSET Inc. was reviewed and approved by the Institutional Animal Care and Use Committee protocol no. I00266 with adherence to the Animal Welfare Act regulations and standards as set by the Office of Laboratory Animal Welfare and the Guide for the Care and Use of Laboratory Animals. The animal safety study performed at Massachusetts Eye and Ear was reviewed and approved by the Animal Care Committee of the Institutional Review Board, protocol 2021 N000103. The ARRIVE (Animal Research: Reporting of In Vivo Experiments) checklist is included in Materials and Methods S14. The number of animals (n = 8) requested in the efficacy study was chosen to demonstrate a 60% relative increase in the mean of the primary outcome or the mass of passively transported drug into the ME within <1 min, at the 0.05 significance level, and with power of 90% using a two-sample t test. Animals' ears were assigned control and test TT at random. Blinding surgical and drug administration procedures was not possible because the researcher would automatically see the tube on the endoscope's screen. Any animals with incomplete healing of the TM around the tube (n = 1, for the SoC-TT) were excluded from analysis. The HPLC-MS measurements were blinded, the sample identifiers were concealed, and the analysis of data was conducted by a separate team blinded to the intervention. Power analysis for all studies was done using G\*Power 3.1.

#### **Fabrication of tubes**

Molds for the production of custom TTs were designed with Fusion360 (Autodesk) (Materials and Methods S5 and fig. S8) and fabricated using an Aureus stereolithography 3D printer (EnvisionTEC). The TTs were named on the basis of the resemblance of their shapes to Greek letters "H," "y," and "x." Medical-grade silicone, MED-4960 (Nusil), was injected into the molds, which were then clamped and cured at 85°C for 2 hours. The TTs were then removed from the molds and heated at 165°C for 5 min to complete the curing process. Each TT was then immersed into 200  $\mu$ l of 100 or 350 cP of medical-grade silicone oil, MED-360 (Nusil), at 25°C for 48 hours. The optimized  $\gamma$ -iTT (ID $_{min}$  = 0.66 mm) with 2% w/w green pigment, MED 4800-6 (Nusil), was manufactured by Albright Silicone.

#### Fabrication of flat silicone sheets

Clean glass slides (VWR) were treated with  $O_2$  plasma for 5 min (Femto PCCE, Diener Electronic) and then placed into a desiccator in the presence of 50  $\mu$ l of trichloro-(1H,1H,2H,2H-perfluorooctyl) silane (97%, Sigma-Aldrich). Four steel rods (~0.32 mm Ø, McMaster-Carr) were placed between two glass slides to serve as spacers. About 500  $\mu$ l of silicone elastomer (MED-4960, Nusil) were injected onto the center of a glass slide and subsequently compressed by a second silanized glass slide. Clamps were placed on the edges to ensure uniformity. The sheets were cured at 165°C for 5 to 7 min.

#### Materials characterization

Exterior and interior dimensions of noninfused and infused TTs were measured using a micro-computed tomography x-ray imaging system, HMXST225 (X-Tek), with a tungsten x-ray source at 70 kV and 80 A. Optical images of noninfused and infused tubes were acquired with a reflectance bright-field microscope, Axio Imager (Zeiss), and with a digital single-lens reflex camera equipped with a macro lens, EF 100 mm f/2.8 L Macro IS USM (Canon).

#### Fluid flow simulations

To derive the optimized H,  $\gamma$ , and  $\chi$ -TT geometries, simulations were carried out using MATLAB (MathWorks) that analytically solve the YL pressure for water and antibiotic drops and calculate the geometrical features (radius, flange angle, and height) on the basis of the selected boundary conditions (see Materials and Methods S1 to S3 for details).

#### **Hydrostatic setup**

Breakthrough pressures for all liquids studied were measured using a custom-built hydrostatic pressure chamber with inserted TT (Fig. 3G, inset i). For each experiment, the chamber was slowly filled with a fluid until the hydrostatic pressure was high enough to penetrate the TT, with the breakthrough pressure determined from the fluid height just before that point (see Materials and Methods S6 for details).

### Bacterial adhesion studies Bacterial isolates and growth conditions

All strains were reconstituted from frozen glycerol stocks on their respective agar plates. MRSA, MC, SP, and PA strains were all grown on 5% sheep blood agar plates, with NTHI being grown on chocolate agar plates supplemented with haemin (Thermo Fisher Scientific) and nicotinamide adenine dinucleotide (Thermo Fisher Scientific).

#### In vitro biofouling assay

Bacterial solutions in phosphate-buffered saline (PBS) were diluted 1:100 in trypticase soy broth (TSB) containing 1.5% NaCl for MRSA, brain heart infusion (BHI) for MC, and supplemented brain heart infusion (sBHI) for NTHI; Luria broth (LB) containing 0.5% citrate for PA; and Todd Hewitt broth (Becton Dickinson) containing 0.5% yeast extract (Becton Dickinson) for SP. Oilinfused silicone discs of MED-4960 (n=9 per strain, 0.50 cm Ø, 0.35  $\pm$  0.05 mm thickness, NuSil) were placed into a 96-well plate. Each well was filled with 200  $\mu$ l of biofilm medium inoculated with the tested isolate. Plates were incubated for 24 hours at 37°C, then stained with 0.5 w/v% CV and rinsed. The remaining dye bound to the samples was solubilized with 7% glacial acetic acid, and its

absorbance was measured at 570 nm using a Biotek Synergy 2 microplate reader (Agilent).

#### Biofilm confocal imaging

Oil-infused sheets [1 cm by 1 cm by 300  $\mu$ m (length by width by height)] of MED-4960 (NuSil) were used as substrates to grow biofilms for confocal imaging (n=9 per strain). Bacterial solutions were diluted to a 1:100 concentration and left to grow for 24 hours in their optimal environments. Afterward, the substrates were rinsed three times with PBS, stained for 15 min with the LIVE/DEAD BacLight Bacterial Viability Kit (Thermo Fisher Scientific, no. L7012), rinsed three times again with PBS, and fixed with 10% neutral buffered formalin solution (Thermo Fisher Scientific). Biofilms were then imaged using a Zeiss LSM700 upright confocal microscope with a  $40\times$  water immersion objective.

#### Cell adhesion studies

#### Cell culture and seeding

HNDFs modified with enhanced green fluorescent protein (eGFP;  $\lambda_{\rm ex}=488$  nm) (Angio-Proteomie, no. AS214583) were cultured in Dulbecco's modified eagle medium supplemented with L-alanyl-glutamine (862 mg liter<sup>-1</sup>; Gibco) and 10% fetal bovine serum [American Type Culture Collection (ATCC)] in an incubator at 37°C with 5% CO<sub>2</sub> atmosphere. Cell medium was prewarmed and replaced every 2 days up to passage 20. At 80% confluency, cells were passaged with 0.05% trypsin–0.53 mM EDTA (Gibco). Primary HEKs from neonatal foreskin (PCS-200-010, ATCC) were cultured in dermal cell basal medium (ATCC) supplemented with a keratinocyte growth kit (ATCC) according to the manufacturer's instructions. Cells were kept in an incubator (VWR) at 37°C with 5% CO<sub>2</sub> atmosphere up to passage 10.

#### Fluorescent confocal imaging

For confocal imaging, HNDFs and HEKs were seeded onto silicone discs for 48 hours in six-well plates at a density of 50,000 cells cm $^{-2}$  (n=3 per cell type). HNDFs were visualized via cytoplasmic eGFP without additional staining. HEK samples were incubated with a PBS solution containing 5  $\mu M$  ethidium homodimer-1 and 2  $\mu M$  calcein-AM for 30 min at 25°C (Thermo Fisher Scientific). Cellular adhesion was then assessed by observing the cell coverage recorded by a confocal scanning laser microscope (LSM700, Zeiss) at 5× magnification.

#### Adhesion force with AFM

For adhesion strength measurements, HNDFs and HEKs were seeded onto sheets of MED-4960 infused with MED-360 100 cP (n=3 per cell type) for 48 hours in 35 mm-by-10 mm petri dishes at a density of 5000 cells cm<sup>-2</sup> for each cell type. The adhesion force of each cell was measured through lateral pull-off as previously reported by Nguyen and Gu (58) using an AFM (NanoWizard 4a, JPK Instruments) with silicon AFM probes (All-In-One-Al, BudgetSensors) at 37°C.

#### In vivo safety studies

Adult female *C. lanigera* (400 to 500 g, n=16) were anesthetized to undergo the myringotomy with TT insertion and further monitoring of TM healing, of which eight animals underwent the ABR testing before myringotomy. TTs were surgically placed into both TMs in the Massachussetts Eye and Ear's Animal Care Facility. In a randomized fashion, one ear received a control SoC-TT (silicone Collar Button, ID = 1.27 mm, VT-1002, Summit Medical), and the other ear received a "test" iTT (350 cP oil-infused silicone TTs with

H geometry with similar dimensions as the SoC tube, ID = 1.28  $\pm$  0.02 mm, or with  $\gamma$  geometry, ID = 0.66  $\pm$  0.01 mm). After the TT placement, the animals were allowed to recover for 2 weeks and were monitored closely with weekly otoendoscopic imaging to document healing around the TT at the myringotomy site.

For ABR testing, the anesthetized animals were placed in a sound-treated booth, and bilateral ABR thresholds were obtained using a broadband click and at 1, 2, 4, 8, and 16 kHz using the Eaton-Peabody Laboratories Cochlear Function Test Suite written in LabVIEW. After ABR, TTs were placed into both ears in the surgical sterile facility. One ear received a control SoC-TT, and the other ear received a test tube (H-iTT or  $\gamma$ -iTTs). After the 2-week recovery period, the animals underwent a second general anesthetic and the second ABR. Afterward, TTs from both ears were removed from the TM under endoscopic guidance. The animals were then permitted to recover for an additional ~12 or ~24 weeks for subsequent ABR tests. Histologic sections of the temporal bones were analyzed using H&E stain with light microscopy at the site of the prior TT. Qualitative analysis of the organ of Corti and Rosenthal's canal was performed to assess inner ear health. Further details are in Methods and Materials S11.

#### In vivo efficacy studies

Adult male C. lanigera (400 to 500 g, n = 8) were anesthetized and underwent myringotomy with TT insertion at CilCare Inc. One ear received a SoC-TT, and the other ear received an optimized  $\gamma$ -iTT, using an identical protocol as described above. After the TM healed around the tube at ~14 days, the animals were deeply anesthetized, and an opening into the posterior tympanic bulla was created. A 30°-angled endoscope was positioned to visualize the medial surface of the TM from the ME. The 0.3% ciprofloxacin and 0.1% dexamethasone otic suspension was introduced into the EAC and allowed time to drain through the tube into the ME. Passive transport was observed for a period of 5 min, and video was recorded. After 5 min, the endoscope was removed, and any otic suspension residual in the EAC was suctioned from around the tube. Thereafter, ME fluid was aspirated from chinchillas through the dorsal aspect of the auditory bulla using a sterile syringe and a 20-gauge needle after three saline (500 µl) serial washes for dilution and to improve extraction efficiency of the therapeutic from the ME cavity. Extracted fluid was then analyzed using HPLC and MS to quantify mass of ciprofloxacin delivered to the ME space. Further details are in Methods and Materials S12.

#### Statistical analysis

All statistical analyses, box and bar graphs, violin, and Kaplan-Meyer plots were prepared using GraphPad Prism 9 as described in the figure captions and in the main text. Data that were normally distributed were described with means and SDs, and comparison between two or more groups was determined using paired, unpaired t tests (with Welch's correction where necessary). Otherwise, comparisons between groups were done using one-way analysis of variance (ANOVA), Mann-Whitney, and log-rank tests. Two-tailed P < 0.05 was considered statistically significant.

#### SCIENCE TRANSLATIONAL MEDICINE | RESEARCH ARTICLE

#### **Supplementary Materials**

This PDF file includes: Materials and Methods S1 to S14 Figs. S1 to S20

Tables S1 to S6 References (59–70)

Other Supplementary Material for this manuscript includes the following:

Movies S1 and S2 MDAR Reproducibility Checklist

View/request a protocol for this paper from Bio-protocol.

#### **REFERENCES AND NOTES**

- R. M. Rosenfeld, D. E. Tunkel, S. R. Schwartz, S. Anne, C. E. Bishop, D. C. Chelius, J. Hackell, L. L. Hunter, K. L. Keppel, A. H. Kim, T. W. Kim, J. M. Levine, M. T. Maksimoski, D. J. Moore, D. A. Preciado, N. P. Raol, W. K. Vaughan, E. A. Walker, T. M. Monjur, Clinical practice guideline: Tympanostomy tubes in children (update). *Otolaryngol. Head Neck Surg.* 166, S1–S55 (2022).
- S. J. Gedde, J. C. Schiffman, W. J. Feuer, L. W. Herndon, J. D. Brandt, D. L. Budenz; Tube versus Trabeculectomy Study Group, Treatment outcomes in the tube versus trabeculectomy (TVT) study after five years of follow-up. Am. J. Ophthalmol. 153, 789–803.e2 (2012).
- J.-M. Dumonceau, A. Tringali, D. Blero, J. Devière, R. Laugiers, D. Heresbach, G. Costamagna, Biliary stenting: Indications, choice of stents and results: European Society of Gastrointestinal Endoscopy (ESGE) clinical guideline. *Endoscopy* 44, 277–298 (2012).
- C. A. Harris, J. P. McAllister 2nd, What we should know about the cellular and tissue response causing catheter obstruction in the treatment of hydrocephalus. *Neurosurgery* 70, 1589–1601 (2012).
- A. G. M. Schilder, T. Chonmaitree, A. W. Cripps, R. M. Rosenfeld, M. L. Casselbrant, M. P. Haggard, R. P. Venekamp, Otitis media. Nat. Rev. Dis. Primer 2, 16063 (2016).
- S. J. Gedde, L. W. Herndon, J. D. Brandt, D. L. Budenz, W. J. Feuer, J. C. Schiffman; Tube Versus Trabeculectomy Study Group, Postoperative complications in the tube versus trabeculectomy (TVT) study during five years of follow-up. *Am. J. Ophthalmol.* 153, 804–814.e1 (2012).
- N. Bhattacharyya, S. G. Shay, Epidemiology of pediatric tympanostomy tube placement in the United States. Otolaryngol. Head Neck Surg. 163, 600–602 (2020).
- 8. M. M. Rovers, The burden of otitis media. Vaccine 26, G2-G4 (2008).
- R. M. Rosenfeld, S. R. Schwartz, M. A. Pynnonen, D. E. Tunkel, H. M. Hussey, J. S. Fichera, A. M. Grimes, J. M. Hackell, M. F. Harrison, H. Haskell, D. S. Haynes, T. W. Kim, D. C. Lafreniere, K. LeBlanc, W. L. Mackey, J. L. Netterville, M. E. Pipan, N. P. Raol, K. G. Schellhase, Clinical practice guideline: Tympanostomy tubes in children. *Otolaryngol. Neck Surg.* 149, S1–S35 (2013).
- D. J. Kay, M. Nelson, R. M. Rosenfeld, Meta-analysis of tympanostomy tube sequelae. Otolaryngol. Head Neck Surg. 124, 374–380 (2001).
- D. E. Conrad, J. R. Levi, Z. A. Theroux, Y. Inverso, U. K. Shah, Risk factors associated with postoperative tympanostomy tube obstruction. *JAMA Otolaryngol. Head Neck Surg.* 140, 727–730 (2014).
- R. L. Hebert 2nd, M. L. Vick, G. E. King, J. P. Bent 3rd, Tympanostomy tubes and otic suspensions: Do they reach the middle ear space? *Otolaryngol. Head Neck Surg.* 122, 330–333 (2000).
- S. Phan, Inner ear drug delivery: Tomorrow's treatment for hearing loss? Hear. J. 72, 22 (2019).
- S. S. Chandrasekhar, B. S. Tsai Do, S. R. Schwartz, L. J. Bontempo, E. A. Faucett,
   A. Finestone, D. B. Hollingsworth, D. M. Kelley, S. T. Kmucha, G. Moonis, G. L. Poling,
   J. K. Roberts, R. J. Stachler, D. M. Zeitler, M. D. Corrigan, L. C. Nnacheta, L. Satterfield, Clinical practice guideline: Sudden hearing loss (update). *Otolaryngol. Head Neck Surg.* 161, S1–S45 (2019).
- X. Hou, Y. Hu, A. Grinthal, M. Khan, J. Aizenberg, Liquid-based gating mechanism with tunable multiphase selectivity and antifouling behaviour. *Nature* 519, 70–73 (2015).
- 16. K. W. Oh, C. H. Ahn, A review of microvalves. J. Micromech. Microeng. 16, R13 (2006).
- N. H. Lin, M.-m. Kim, G. T. Lewis, Y. Cohen, Polymer surface nano-structuring of reverse osmosis membranes for fouling resistance and improved flux performance. *J. Mater. Chem.* 20, 4642–4652 (2010).
- N. Adrus, M. Ulbricht, Novel hydrogel pore-filled composite membranes with tunable and temperature-responsive size-selectivity. J. Mater. Chem. 22, 3088–3098 (2012).

- R. L. Whelan, R. C. Maguire, Tympanostomy tube innovation: Advances in device material, design, and office-based technology. Ear Nose Throat J. 99, 485–50S (2020).
- A. R. Barron, Universal approximation bounds for superpositions of a sigmoidal function. *IEEE Trans. Inf. Theory* 39, 930–945 (1993).
- M. E. Tavin, M. Gordon, R. J. Ruben, Hearing results with the use of different tympanostomy tubes: A prospective study. Int. J. Pediatr. Otorhinolaryngol. 15, 39–50 (1988).
- G. Isaacson, Tympanostomy tubes-A visual guide for the young otolaryngologist. Ear Nose Throat J. 99, 85–14S (2020).
- R.T. Younis, Prevention and treatment of plugged tympanostomy tubes. Ear Nose Throat J. 86, 21–23 (2007).
- J.-J. Song, I. Noh, S.-W. Chae, Inhibition of biofilm formation on ventilation tubes by surface modification. *In Vivo* 26, 907–911 (2012).
- T. D. Morgan, M. Wilson, The effects of surface roughness and type of denture acrylic on biofilm formation by Streptococcus oralis in a constant depth film fermentor. J. Appl. Microbiol. 91, 47–53 (2001).
- 26. T. Young, An essay on the cohesion of fluids. Philos. Trans. R. Soc. Lond. 95, 65-87 (1805).
- P. S. de Laplace, Traité De Mécanique Céleste: Supplément au dixième livre du traité de méchanique céleste sur l'action capillaire (Duprat, 1806).
- M. J. Kreder, D. Daniel, A. Tetreault, Z. Cao, B. Lemaire, J. V. I. Timonen, J. Aizenberg, Film dynamics and lubricant depletion by droplets moving on lubricated surfaces. *Phys. Rev. X* 8, 031053 (2018).
- T.-S. Wong, S. H. Kang, S. K. Y. Tang, E. J. Smythe, B. D. Hatton, A. Grinthal, J. Aizenberg, Bioinspired self-repairing slippery surfaces with pressure-stable omniphobicity. *Nature* 477, 443–447 (2011).
- M. Villegas, Y. Zhang, N. Abu Jarad, L. Soleymani, T. F. Didar, Liquid-infused surfaces: A review of theory, design, and applications. ACS Nano 13, 8517–8536 (2019).
- D. Daniel, J. V. I. Timonen, R. Li, S. J. Velling, J. Aizenberg, Oleoplaning droplets on lubricated surfaces. *Nat. Phys.* 13, 1020–1025 (2017).
- M. J. Kreder, J. Alvarenga, P. Kim, J. Aizenberg, Design of anti-icing surfaces: Smooth, textured or slippery? *Nat. Rev. Mater.* 1, 15003 (2016).
- F. Schellenberger, J. Xie, N. Encinas, A. Hardy, M. Klapper, P. Papadopoulos, H.-J. Butt, D. Vollmer, Direct observation of drops on slippery lubricant-infused surfaces. Soft Matter 11, 7617–7626 (2015).
- J. Feng, M. Muradoglu, H. Kim, J. T. Ault, H. A. Stone, Dynamics of a bubble bouncing at a liquid/liquid/gas interface. J. Fluid Mech. 807, 324–352 (2016).
- C. Howell, A. Grinthal, S. Sunny, M. Aizenberg, J. Aizenberg, Designing liquid-infused surfaces for medical applications: A review. Adv. Mater. 30, 1802724 (2018).
- D. C. Leslie, A. Waterhouse, J. B. Berthet, T. M. Valentin, A. L. Watters, A. Jain, P. Kim,
   D. Hatton, A. Nedder, K. Donovan, E. H. Super, C. Howell, C. P. Johnson, T. L. Vu,
   E. Bolgen, S. Rifai, A. R. Hansen, M. Aizenberg, M. Super, J. Aizenberg, D. E. Ingber, A bioinspired omniphobic surface coating on medical devices prevents thrombosis and biofouling. *Nat. Biotechnol.* 32, 1134–1140 (2014).
- J. Chen, C. Howell, C. A. Haller, M. S. Patel, P. Ayala, K. A. Moravec, E. Dai, L. Liu, I. Sotiri, M. Aizenberg, J. Aizenberg, E. L. Chaikof, An immobilized liquid interface prevents device associated bacterial infection in vivo. *Biomaterials* 113, 80–92 (2017).
- I. Sotiri, J. C. Overton, A. Waterhouse, C. Howell, Immobilized liquid layers: A new approach to anti-adhesion surfaces for medical applications. Exp. Biol. Med. (Maywood) 241, 909–918 (2016)
- A. K. Epstein, T.-S. Wong, R. A. Belisle, E. M. Boggs, J. Aizenberg, Liquid-infused structured surfaces with exceptional anti-biofouling performance. *Proc. Natl. Acad. Sci. U.S.A.* 109, 13182–13187 (2012).
- S. Amini, S. Kolle, L. Petrone, O. Ahanotu, S. Sunny, C. N. Sutanto, S. Hoon, L. Cohen, J. C. Weaver, J. Aizenberg, N. Vogel, A. Miserez, Preventing mussel adhesion using lubricant-infused materials. Science 357, 668–673 (2017).
- N. Juthani, C. Howell, H. Ledoux, I. Sotiri, S. Kelso, Y. Kovalenko, A. Tajik, T. L. Vu, J. J. Lin, A. Sutton, J. Aizenberg, Infused polymers for cell sheet release. Sci. Rep. 6, 26109 (2016).
- 42. T. Marom, N. Habashi, R. Cohen, S. O. Tamir, Role of biofilms in post-tympanostomy tube otorrhea. *Ear Nose Throat J.* **99**, 225–295 (2020).
- J. Dohar, Microbiology of otorrhea in children with tympanostomy tubes: Implications for therapy. Int. J. Pediatr. Otorhinolaryngol. 67, 1317–1323 (2003).
- A. Ruohola, O. Meurman, S. Nikkari, T. Skottman, A. Salmi, M. Waris, R. Österback, E. Eerola, T. Allander, H. Niesters, T. Heikkinen, O. Ruuskanen, Microbiology of acute otitis media in children with tympanostomy tubes: Prevalences of bacteria and viruses. *Clin. Infect. Dis.* 43, 1417–1422 (2006).
- C. C. Ngo, H. M. Massa, R. B. Thornton, A. W. Cripps, Predominant bacteria detected from the middle ear fluid of children experiencing otitis media: A systematic review. PLOS ONE 11, e0150949 (2016).

#### SCIENCE TRANSLATIONAL MEDICINE | RESEARCH ARTICLE

- J. Qiu, Y. Wang, W. Guo, L. Xu, Y. Mou, L. Cui, F. Han, Y. Sun, Role of TGF-β1-mediated epithelial-mesenchymal transition in the pathogenesis of tympanosclerosis. *Exp. Ther. Med.* 21. 6 (2021).
- B. Giles, Wound healing in spontaneous perforation or myringotomy and middle ear reconstruction. Ear Nose Throat J. 86. 30–32 (2007).
- H. Joe, Y. J. Seo, A newly designed tympanostomy stent with TiO<sub>2</sub> coating to reduce Pseudomonas aeruginosa biofilm formation. J. Biomater. Appl. 33, 599–605 (2018).
- J. Malaty, P. J. Antonelli, Effect of blood and mucus on tympanostomy tube biofilm formation. *Laryngoscope* 118, 867–870 (2008).
- J. Sapudom, S. Rubner, S. Martin, S. Thoenes, U. Anderegg, T. Pompe, The interplay of fibronectin functionalization and TGF-β1 presence on fibroblast proliferation, differentiation and migration in 3D matrices. *Biomater. Sci.* 3, 1291–1301 (2015).
- J. Cui, Z. Li, C. Jin, Z. Jin, Knockdown of fibronectin extra domain B suppresses TGF-β1mediated cell proliferation and collagen deposition in keloid fibroblasts via AKT/ERK signaling pathway. *Biochem. Biophys. Res. Commun.* 526, 1131–1137 (2020).
- G. C. Hunt, P. Singh, J. E. Schwarzbauer, Endogenous production of fibronectin is required for self-renewal of cultured mouse embryonic stem cells. *Exp. Cell Res.* 318, 1820–1831 (2012).
- M. Yoshikawa, H. Kojima, Y. Yaguchi, N. Okada, H. Saito, H. Moriyama, Cholesteatoma fibroblasts promote epithelial cell proliferation through overexpression of epiregulin. PLOS ONE 8, e66725 (2013).
- T. Pawelczyk, M. Sakowicz-Burkiewicz, M. Wesserling, M. Grden, J. Kuczkowski, Altered response of fibroblasts from human tympanosclerotic membrane to interacting mast cells: Implication for tissue remodeling. *Int. J. Biochem. Cell Biol.* 57, 35–44 (2014).
- I. Valiente-Alandi, S. J. Potter, A. M. Salvador, A. E. Schafer, T. Schips, F. Carrillo-Salinas, A. M. Gibson, M. L. Nieman, C. Perkins, M. A. Sargent, J. Huo, J. N. Lorenz, T. DeFalco, J. D. Molkentin, P. Alcaide, B. C. Blaxall, Inhibiting fibronectin attenuates fibrosis and improves cardiac function in a model of heart failure. *Circulation* 138, 1236–1252 (2018).
- A. Vishwakarma, N. S. Bhise, M. B. Evangelista, J. Rouwkema, M. R. Dokmeci,
   A. M. Ghaemmaghami, N. E. Vrana, A. Khademhosseini, Engineering immunomodulatory biomaterials to tune the inflammatory response. *Trends Biotechnol.* 34, 470–482 (2016).
- M. Bont, C. Barry, S. Johnston, A review of liquid silicone rubber injection molding: Process variables and process modeling. *Polym. Eng. Sci.* 61, 331–347 (2021).
- T. D. Nguyen, Y. Gu, Investigation of cell-substrate adhesion properties of living chondrocyte by measuring adhesive shear force and detachment using AFM and inverse FEA. Sci. Rep. 6, 38059 (2016).
- 59. N. J. Marks, R. P. Mills, Swimming and Grommets. J. R. Soc. Med. 76, 23–26 (1983).
- J. Subtil, N. Martins, T. Nunes, D. Covas, P. Vera-Cruz, R. Voegels, J. Paco, Including auditory tube function on models is relevant to assess water exposure after tympanostomy tubes-Multiphase computerized fluid dynamics model. *Int. J. Pediatr. Otorhinolaryngol.* 111, 187–191 (2018).
- 61. R. Mauri, Transport Phenomena in Multiphase Flows (Springer, 2015).
- 62. A. B. D. Cassie, Contact angles. Discuss. Faraday Soc. 3, 11-16 (1948).
- H. P. Meissner, A. S. Michaels, Surface tensions of pure liquids and liquid mixtures. *Ind. Eng. Chem.* 41, 2782–2787 (1949).
- S. Val, M. Poley, K. Anna, G. Nino, K. Brown, M. Pérez-Losada, H. Gordish-Dressman,
   D. Preciado, Characterization of mucoid and serous middle ear effusions from patients with chronic otitis media: Implication of different biological mechanisms? *Pediatr. Res.* 84, 296–305 (2018).
- C. Howell, T. L. Vu, J. J. Lin, S. Kolle, N. Juthani, E. Watson, J. C. Weaver, J. Alvarenga, J. Aizenberg, Self-replenishing vascularized fouling-release surfaces. ACS Appl. Mater. Interfaces 6, 13299–13307 (2014).

- J. C. Wang, A. N. Hamood, C. Saadeh, M. J. Cunningham, M. T. Yim, J. Cordero, Strategies to prevent biofilm-based tympanostomy tube infections. *Int. J. Pediatr. Otorhinolaryngol.* 78, 1433–1438 (2014)
- S. O. Tamir, T. Marom, B. Zaks, D. Steinberg, Pseudomonal biofilm topographic distribution on tympanostomy tubes: An in vitro model. *Pediatr. Infect. Dis. J.* 35, 1357–1360 (2016).
- J. Cheng, L. Javia, Methicillin-resistant Staphylococcus aureus (MRSA) pediatric tympanostomy tube otorrhea. *Int. J. Pediatr. Otorhinolaryngol.* 76, 1795–1798 (2012).
- S. K. Lee, M. S. Lee, S. Y. Jung, J. Y. Byun, M. S. Park, S. G. Yeo, Antimicrobial resistance of Pseudomonas aeruginosa from otorrhea of chronic suppurative otitis media patients. Otolaryngol. Head Neck Surg. 143, 500–505 (2010).
- D. R. Trakimas, R. Ishai, I. Ghanad, N. L. Black, E. D. Kozin, J. T. Cheng, A. K. Remenschneider, Otopathologic evaluation of temporalis fascia grafts following successful tympanoplasty in humans. *Laryngoscope* 128, E351–E358 (2018).

Acknowledgments: We would like to thank S. Peppou-Chapman, C. W. Visser, C. N. Kaplan, S. Brandt, M. C. Fernandes, A. Pawlowski, A. Rudolph, M. Aizenberg, K. Bertoldi, D. Lee, D. Preciado, and S. Sunny for discussions and suggestions as well as D. Gandhi and M. Castillo Bustamante for clinical expertise. We thank T. Blough, B. Freedman, E. S. Wang, A. Stowman, S. Uzel, M. Skylar Scott, K. Mason, and M.-C. Le for experimental assistance. We appreciate the biostatistical support by G. Fitzmaurice from Harvard Catalyst and the Harvard Clinical and Translational Science Center (National Center for Advancing Translational Sciences, National Institutes of Health Award UL1 TR002541) and financial contributions from Harvard University and its affiliated academic health care centers. We thank A. Marie and C. Sage at CILcare Inc. and CBSET Inc. for assisting with the efficacy study in chinchillas. Funding: This work was supported by the Wyss Institute validation project funding (to J. Aizenberg and A.K.R.) and by the National Science Foundation (NSF) through the Harvard University Materials Research Science and Engineering Center (MRSEC) under award number DMR-2011754 (to J. Aizenberg and J.A.L.). Research reported in this publication was also supported by the National Institute on Deafness and Other Communication Disorders of the National Institutes of Health under award number R43DC019318 (to I.P., A.K.R., and E.D.K.) and award number K08 - K08DC018575 (to A.K.R.). The content is solely the responsibility of the authors and does not necessarily represent the official views of the National Institutes of Health, Author contributions: I.P., H.P., E.D.K., J. Aizenberg, and A.K.R. conceptualized the research. I.P., H.P., J.A.L., P.J.M.B., E.D.K., J. Aizenberg, and A.K.R. supervised the studies. I.P., H.P., J. Alvarenga, C.T.Z., N.L.B., Q.J., C.W.F.L., J.C., Z.L., J.C.W., and P.J.M.B. developed the methodology and performed the experiments. H.P. and M.J.K. performed computational modeling. I.P., J. Aizenberg, and A.K.R. acquired the funding. I.P. and H.P. visualized data and created figures, I.P., H.P., A.G., J. Aizenberg, and A.K.R. wrote the manuscript. Competing interests: I.P. and J. Aizenberg are cofounders of PionEar Technologies Inc. J. Aizenberg, N.L.B., E.D.K., M.J.K., H.P., I.P., and A.K.R. are listed as inventors on the patent application US20210052428 "Designs for tympanostomy conduits or subannular ventilation conduits and other medical and fluidic conduits" and J. Aizenberg, H.P., I.P., and C.T.Z. on PCT/ US2021/048060 "Drug combination kits and methods of drug delivery" related to the work described herein. E.D.K., A.K.R., and J.A.L. serve on the Scientific Advisory Board for Desktop Metal, J.A.L. also serves on the Scientific Advisory Boards of Autodesk, Azul 3D, Mooii Meat, Reel Seafood, and Trestle Biotherapeutics and is a scientific cofounder of Acoustica Bio. All other authors declare that they have no competing interests. Data and materials availability: All data associated with this study are present in the paper or the Supplementary Materials.

Submitted 16 July 2022 Resubmitted 08 December 2022 Accepted 13 March 2023 Published 5 April 2023 10.1126/scitranslmed.add9779

## **Science** Translational Medicine

#### Design of medical tympanostomy conduits with selective fluid transport properties

Haritosh Patel, Ida Pavlichenko, Alison Grinthal, Cathy T. Zhang, Jack Alvarenga, Michael J. Kreder, James C. Weaver, Qin Ji, Christopher W.F. Ling, Joseph Choy, Zihan Li, Nicole L. Black, Paulo J.M. Bispo, Jennifer A. Lewis, Elliott D. Kozin, Joanna Aizenberg, and Aaron K. Remenschneider

Sci. Transl. Med., **15** (690), eadd9779. DOI: 10.1126/scitranslmed.add9779

#### View the article online

https://www.science.org/doi/10.1126/scitranslmed.add9779

#### **Permissions**

https://www.science.org/help/reprints-and-permissions

Use of this article is subject to the Terms of service